Lattice Boltzmann method coupled with the Oldroyd-B constitutive model for a viscoelastic fluid

Jin Su,[1] Jie Ouyang,[1,*] Xiaodong Wang,[1] and Binxin Yang[2]
[1]*School of Science, Northwestern Polytechnical University, Xi'an 710129, Shaanxi, PR China*
[2]*School of Applied Science, Taiyuan University of Science and Technology, Taiyuan 030024, Shanxi, PR China*
(Received 9 June 2013; published 4 November 2013)

We developed a lattice Boltzmann method coupled with the Oldroyd-B constitutive equation to simulate a viscoelastic fluid. In this work, the flow field of the solvent is solved using an incompressible lattice Boltzmann Bhatnagar-Gross-Krook (BGK) model, while the advection operator of the polymer stress tensor is directly calculated with the help of the particle distribution functions. Specifically, we present a numerical scheme for the advection of the polymer stress tensor through the truncation of second-order Taylor expansion, which does not need to introduce the extra distribution functions and has better numerical accuracy. We consider two types of numerical tests to examine the performance of the presented method, including a two-dimensional (2D) channel flow and the 4:1 contraction problem. Our numerical results for the 2D channel flow agree well with the analytical results and some experimental results reported in the previous studies. Moreover, the numerical results also indicate that the current method can capture some complex rheological behaviors of the 4:1 contraction flow.

DOI: 10.1103/PhysRevE.88.053304 PACS number(s): 47.11.Qr, 47.57.Ng

I. INTRODUCTION

Viscoelastic fluids have a wide range of applications in science and engineering, such as plastics and pharmaceuticals. Different from the Newtonian fluid, the stress of a viscoelastic fluid depends on not only the stress impressed at present, but also the one impressed during the previous deformation history of the fluid. So viscoelastic fluids can exhibit quite different flow behaviors from those of the Newtonian fluids in many aspects, such as rod climbing, siphoning, and secondary flows. In many engineering applications, the numerical simulation has become an effective technique to predict the performance of viscoelastic fluid. Among various numerical methods, the lattice Boltzmann method (LBM) [1–3] is generally regarded as a mecroscopic method that lies between microscopic and macroscopic methods. Compared with the conventional computational approach, the LBM is easy in programming and parallelization because it is explicit and does not need to solve the Poisson equation for pressure [3]. In addition, the kinetic nature of LBM also has an advantage of simulating the complex phenomena of viscoelastic fluid.

During the last two decades, great efforts have been made in developing the LBM for viscoelastic fluid. In an earlier study, Qian and Deng [4] imposed the elastic effect into LBM by modifying the equilibrium distribution. Later, Giraud *et al*. [5,6] and Lallemand *et al*. [7] proposed a scheme coupled with the Jeffreys model, but they assumed that the stress tensor was traceless and essentially linear without considering some important elastic effect. Wagner *et al*. [8] extended the LBM to simulate a cusped bubble rising in a viscoelastic fluid. Ispolatov and Grant [9] considered the elastic effect by adding a Maxwell-like (exponentially decaying) force into the lattice Boltzmann equation, but they also did not pay attention to the important elastic effect. Subsequently, Onishi [10] and Ammar [11] combined the LBM with the polymer kinetic theory which was described by the Fokker-Planck equation. Their numerical results were only obtained for homogeneous shear flow and the viscoelastic effect was not allowed to be very strong. For more details about the LBM of viscoelastic fluid, one could refer to Ref. [12] where the full review was provided.

Recently, Malaspinasa *et al*. [13] have described a coupled LBM to simulate the Oldroyd-B fluid flow using two types of distribution functions, which was similar to the ideas of Denniston *et al*. [14] and Spencer *et al*. [15] applied in the liquid crystals. Later, Su *et al*. [16] presented an improved scheme with double-type particle speeds to concern the complex fluid like the high Weissenberg number problem encountered in the lid-driven cavity. In these methodologies mentioned above, two types of distribution functions were defined, one was the scalar density for the momentum and the other was the tensor density for the stress tensor. Although some of these studies show the positive results, there are still some issues. First, one needs to design suitable boundary conditions for the tensor density of the stress tensor evolution. Second, the numerical model requires the extra introduction of distribution functions for the stress tensor, which leads to the large computer memory to store all the distribution functions.

Different from the LBM of Refs. [13] and [14], Karpikov [17] has proposed a lattice Boltzmann scheme coupled with the FENE constitutive model by using a single distribution function to study the turbulence of the non-Newtonian fluid. Karpikov defined a scalar density distribution function for the flow field in his method, and calculated the advection operator of the stress tensor by taking advantage of the scalar density distribution function. Unfortunately, although Karpikov's scheme could avoid bringing in some extra sets of distribution functions, there remains some disadvantages such as the serious numerical dissipation. To obtain a better numerical accuracy, we present a numerical scheme for the advection operator of the stress tensor evolution through treating the system by Taylor series expansion in this paper, which can ease the numerical dissipation of the simulation. Moreover, since there is no extra memory requirement for the stress distribution, the new numerical method allows us to cope with the large system of complex fluids. To examine the actual reliability evaluation of the presented method, we consider two numerical tests including a 2D channel flow

*Corresponding author: jieouyang@nwpu.edu.cn

and the 4:1 contraction problem. It is well known that the contraction flow can be recognized as an ideal benchmark problem for both the experimental and numerical studies of complex viscoelastic fluid, because it has the singularity points near the corners. To our knowledge, there are few reports about the LBM for the Oldroyd-B fluid in contraction geometry. So we also try to simulate this stringent test by using the coupled LBM presented in this paper.

The outline of this paper is organized as follows. Section II describes the mathematical models of viscoelastic fluid. In Sec. III we give the coupled LBM with the Oldroyd-B constitutive equation by using a single distribution function for viscoelastic fluid. In Sec. IV we show the numerical results of the viscoelastic fluid described by the Oldroyd-B model in a 2D channel flow and the 4:1 contraction flow. Finally, in Sec. V we put forward the conclusions and suggestions on this paper.

II. THE MATHEMATICAL MODEL

In our simulations, to consider the important elastic effect, the viscoelastic behavior is modeled by the Oldroyd-B constitutive equation, which can be derived from the kinetic theory of the polymer dilute solution [18]. Here we take the incompressible flow at low Reynolds number as a solvent model. The governing equations of the incompressible momentum conservation are

$$\rho_0\left[\frac{\partial \mathbf{u}}{\partial t}+(\mathbf{u}\cdot\nabla)\mathbf{u}\right]=-\nabla p+\eta_s\nabla^2\mathbf{u}+\nabla\cdot\boldsymbol{\tau}, \tag{1}$$

the equations of the mass conservation are

$$\nabla\cdot\mathbf{u}=0, \tag{2}$$

where p,$\mathbf{u}$,$\boldsymbol{\tau}$ are, respectively, the pressure, velocity, and viscoelastic stress tensor, the latter accounts for the effects of the polymers, and ρ_0 is the density. The Oldroyd-B constitutive equation is given as follows:

$$\lambda_p\frac{D\boldsymbol{\tau}}{Dt}=\lambda_p[\boldsymbol{\tau}\cdot\nabla\mathbf{u}+(\nabla\mathbf{u})^T\cdot\boldsymbol{\tau}]-\boldsymbol{\tau}+2\eta_p\mathbf{d}, \tag{3}$$

where $\frac{D\boldsymbol{\tau}}{Dt}=\frac{\partial\boldsymbol{\tau}}{\partial t}+(\mathbf{u}\cdot\nabla)\boldsymbol{\tau}$ is the material derivative; the superscript T denotes the transpose operation; η_s and η_p are the solvent and polymer viscosities, λ_p is the relaxation time of the polymer solute, and $\mathbf{d}=\frac{1}{2}(\nabla\mathbf{u}+\nabla\mathbf{u}^T)$ is the rate of strain tensor. To characterize the viscoelastic interaction, we define three nondimensional numbers, namely, the Reynolds number (Re), the Weissenberg (Wi) number, and the kinematic viscosity ratio β. The parameter $\beta=\eta_s/\eta_t$ is the ratio of the solvent viscosity to the total, $\eta_t=\eta_s+\eta_p$. The Re number and Wi number are, respectively, $\mathrm{Re}=\rho UL/\eta_t$ and $\mathrm{Wi}=\lambda_p U/L$. U and L are, respectively, the characteristic velocity and length of the flow.

III. THE NUMERICAL ALGORITHM

In this section we aim to describe the numerical implementations of the viscoelastic fluid. As mentioned in the Introduction, there are two types of equations to be considered which are closely coupled with each other. The flow field of solvent is simulated using the 2D incompressible lattice Boltzmann BGK model, whereas the constitutive equation is decoupled as the advection and relaxation-stretching operators with the explicit Euler scheme of time marching. In the present method, the advection operator of the polymer stress tensor can be direct calculated by taking advantage of the particle distribution functions of flow. Specifically, we give a new numerical scheme for the advection of the polymer stress tensor, through treating the system by Taylor series expansion. The present method not only avoids introducing extra sets of distribution functions, but also can improve the numerical accuracy of simulation. The effect of elastic force is incorporated by adding the extra body force into the lattice Boltzmann equation. The asynchronously coupled scheme is used for time marching of the coupled system. We will describe all these contents in detail as follows.

A. 2D incompressible LBGK model

First, let us describe how to integrate the Navier-Stokes equations with the 2D incompressible lattice Boltzmann BGK model (LBGK) [19]. We consider the two-dimensional nine velocity (D2Q9) model, which is shown in Fig. 1. The particle velocity $\mathbf{e}_\alpha$ may be written as

$$\mathbf{e}_\alpha=\begin{cases}(0,0), & \alpha=0,\\ c\left\{\cos\left[(\alpha-1)\frac{\pi}{2}\right],\sin\left[(\alpha-1)\frac{\pi}{2}\right]\right\}, & \alpha=1,2,3,4,\\ \sqrt{2}c\left\{\cos\left[(2\alpha-1)\frac{\pi}{4}\right],\sin\left[(2\alpha-1)\frac{\pi}{4}\right]\right\}, & \alpha=5,6,7,8,\end{cases} \tag{4}$$

where $c=\frac{\delta x}{\delta t}$ is the particle velocity, δx is the lattice grid spacing, and δt is the time step, respectively.

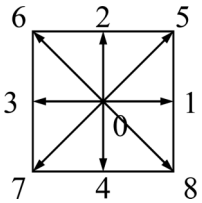

FIG. 1. D2Q9 lattice.

The lattice Boltzmann equation (LBE) reads

$$f_\alpha(\mathbf{x}+\mathbf{e}_\alpha\delta t,t+\delta t)-f_\alpha(\mathbf{x},t)=\Omega_\alpha(f(\mathbf{x},t)), \tag{5}$$

where $f_\alpha(\mathbf{x},t)$ is the distribution function at node $\mathbf{x}$ at time t, $\Omega_\alpha(f(\mathbf{x},t))$ is the BGK collision model

$$\Omega_\alpha(f(\mathbf{x},t))=-\frac{1}{\lambda}\left[f_\alpha(\mathbf{x},t)-f_\alpha^{(\mathrm{eq})}(\mathbf{x},t)\right], \tag{6}$$

where $\lambda=\lambda_0/\delta t$ is the dimensionless relaxation time, λ_0 is relaxation time, and $f_\alpha^{(\mathrm{eq})}$ is the equilibrium distribution

function (EDF) defined as

$$f_\alpha^{(\mathrm{eq})}(\mathbf{x},t) \equiv E_\alpha(\mathbf{u}) = \begin{cases} \rho_0\left[1-(1-\omega_0)\frac{p}{\rho_0 c_s^2}+s_0(\mathbf{u})\right], & \alpha=0, \\ \rho_0\left[\omega_\alpha \frac{p}{\rho_0 c_s^2}+s_\alpha(\mathbf{u})\right], & \alpha=1,\ldots,8, \end{cases} \tag{7}$$

where

$$s_\alpha(\mathbf{u}) = \omega_\alpha\left[\frac{\mathbf{e}_\alpha\cdot\mathbf{u}}{c_s^2}+\frac{(\mathbf{e}_\alpha\cdot\mathbf{u})^2}{2c_s^4}-\frac{\mathbf{u}\cdot\mathbf{u}}{2c_s^2}\right], \tag{8}$$

the weight coefficients are

$$\omega_0=\frac{4}{9},\quad \omega_1,\ldots,\omega_4=\frac{1}{9},\quad \omega_5,\ldots,\omega_8=\frac{1}{36},\quad c_s^2=\frac{c^2}{3}, \tag{9}$$

and $c_s = c/\sqrt{3}$ is the speed of sound, p and $\mathbf{u}$ are the fluid pressure and velocity, respectively. ρ_0 is a constant. The macroscopic velocity and pressure of flow are computed from the distribution functions

$$\rho_0 = \sum_{\alpha=1}^{8} f_\alpha(\mathbf{x}),\quad \rho_0\mathbf{u} = \sum_{\alpha=1}^{8}\mathbf{e}_\alpha f_\alpha(\mathbf{x}), \tag{10}$$

$$p = \frac{\rho_0 c_s^2}{1-\omega_0}\left[\sum_{\alpha=1}^{8} f_\alpha(\mathbf{x})+s_0(\mathbf{u})\right]. \tag{11}$$

Through the Chapman-Enskog expansion, the incompressible Navier-Stokes equations can be recovered as

$$\nabla\cdot\mathbf{u}=0, \tag{12}$$

$$\frac{\partial\mathbf{u}}{\partial t}+\mathbf{u}\cdot\nabla\mathbf{u} = -\nabla P+\nu\nabla^2\mathbf{u}, \tag{13}$$

with the kinematic viscosity $\nu = c_s^2(\lambda-1/2)\delta t$ and $P = p/\rho_0$.

B. Implementation of the Oldroyd-B constitutive model with LBM

As described in Sec. II, the viscoelastic behavior is modeled by the Oldroyd-B constitutive equation (3). For convenience, the constitutive equation could be written as

$$\frac{\partial\boldsymbol{\tau}}{\partial t}+\mathbf{A}_{\mathrm{adv}}(\boldsymbol{\tau},t) = \mathbf{A}_{\mathrm{rel-str}}(\boldsymbol{\tau},t), \tag{14}$$

where the advection and relaxation-stretching operators applied to the polymer stress tensor $\boldsymbol{\tau}$ are respectively given as

$$\mathbf{A}_{\mathrm{adv}}(\boldsymbol{\tau},t) = (\mathbf{u}\cdot\nabla)\boldsymbol{\tau}, \tag{15}$$

$$\mathbf{A}_{\mathrm{rel-str}}(\boldsymbol{\tau},t) = [\boldsymbol{\tau}\cdot\nabla\mathbf{u}+(\nabla\mathbf{u})^T\cdot\boldsymbol{\tau}]+\frac{1}{\lambda_p}(2\eta_p\mathbf{d}-\boldsymbol{\tau}). \tag{16}$$

Here we define the variables of the constitutive equation on the same grid points as the flow. To exchange the information of polymer stress tensors with all neighboring fluid cells, the advection operator needs to be computed by subtracting the outgoing distribution functions of the flow field from the incoming. In the previous study [17], Karpikov has given a simple discretization of the advection operator with the help of the particle distribution functions, which depended on the LBM proposed by Qian *et al.* [12]. Using the same deviating process of Karpikov's method, a numerical scheme of the advection operator based on the incompressible lattice Boltzmann BGK by Guo *et al.* [19] is given as

$$\delta t\,\mathbf{A}_{\mathrm{adv}}(\boldsymbol{\tau},t) = \sum_{\alpha=1}^{m}\boldsymbol{\tau}(\mathbf{x}-\mathbf{e}_\alpha\delta t,t)f_\alpha(\mathbf{x}-\mathbf{e}_\alpha\delta t,t) - \sum_{\alpha=1}^{m}\boldsymbol{\tau}(\mathbf{x},t)f_\alpha(\mathbf{x},t), \tag{17}$$

which is also referred to as Karpikov's scheme in this paper. Through the numerical test, scheme (17) was found to be able to get stable solutions. However, the scheme of Eq. (17) is of lower-order accuracy and larger numerical dissipation. To overcome those shortcomings, we introduce a new numerical scheme for the advection operator. In this new scheme, the advection operator of polymer stress is calculated by

$$\delta t\,\mathbf{A}_{\mathrm{adv}}(\boldsymbol{\tau},t) = 2\sum_{\alpha=1}^{m}\boldsymbol{\tau}(\mathbf{x}-\mathbf{e}_\alpha\delta t,t)f_\alpha(\mathbf{x}-\mathbf{e}_\alpha\delta t,t) - 0.5\sum_{\alpha=1}^{m}\boldsymbol{\tau}(\mathbf{x}-2\mathbf{e}_\alpha\delta t,t)f_\alpha(\mathbf{x}-2\mathbf{e}_\alpha\delta t,t) - 1.5\sum_{\alpha=1}^{m}\boldsymbol{\tau}(\mathbf{x},t)f_\alpha(\mathbf{x},t). \tag{18}$$

Comparing Eq. (18) with Eq. (17), we find that our new scheme differs from Karpikov's model by adding the term

$$0.5\sum_{\alpha=1}^{m}\boldsymbol{\tau}(\mathbf{x},t)f_\alpha(\mathbf{x},t) - \sum_{\alpha=1}^{m}\boldsymbol{\tau}(\mathbf{x}-\mathbf{e}_\alpha\delta t,t)f_\alpha(\mathbf{x}-\mathbf{e}_\alpha\delta t,t) + 0.5\sum_{\alpha=1}^{m}\boldsymbol{\tau}(\mathbf{x}-2\mathbf{e}_\alpha\delta t,t)f_\alpha(\mathbf{x}-2\mathbf{e}_\alpha\delta t,t). \tag{19}$$

This added term is a significant feature of the new scheme (18), which can ease the numerical dissipation. In addition, the new scheme of the advection operator has fairly good numerical stability, because $f_\alpha(\mathbf{x},t)$ is used to handle the convection part along the direction of the particle velocity (namely characteristic direction). The present scheme (18) can be acquired by truncating appropriately the Taylor series expansion of the system. The derivation of the new scheme for the advection operator is shown in the Appendix. We will make some comparisons between Karpikov's scheme and the present scheme for some certain cases in Sec. IV.

For the relaxation-stretching operator $\mathbf{A}_{\mathrm{rel-str}}(\boldsymbol{\tau},t)$, the polymers are stretched by the velocity gradient tensor. The velocity field is computed by constructing the local equilibrium distribution function in each cell, and the derivatives of the velocity are calculated as

$$\frac{\partial u_\alpha}{\partial x_\beta} = \frac{1}{2\delta x}\sum_{i=0}^{8}u_\alpha(\mathbf{x}+\mathbf{e}_i,t)(\mathbf{e}_i)_\beta. \tag{20}$$

Substituting either of the advection and relaxation-stretching operators into the constitutive equation (3), one can

obtain a semidiscrete form which may be compactly written as

$$\frac{\partial \boldsymbol{\tau}}{\partial t} \equiv L(\boldsymbol{\tau}), \tag{21}$$

where the right-hand side of $L(\boldsymbol{\tau})$ contains all the discrete advection and relaxation-stretching operators of the polymer stress tensor. In this work, the time stepping employs the explicit Euler method, namely

$$\frac{\partial}{\partial t}\boldsymbol{\tau}(\mathbf{x},t) = \frac{\boldsymbol{\tau}(\mathbf{x},t+\Delta t)-\boldsymbol{\tau}(\mathbf{x},t)}{\Delta t} = L(\boldsymbol{\tau}). \tag{22}$$

Note that Δt may be different from δt for the LBGK model of flow, and the velocity field is frozen during the time marching of the constitutive equation from n to $n+1$ time steps. Thus, according to Eqs. (18) and (22), the temporal evolution of the stress tensor is given by

$$\begin{aligned}
&\boldsymbol{\tau}(\mathbf{x},t+\Delta t)\\
&\quad = \boldsymbol{\tau}(\mathbf{x},t) + \frac{\Delta t}{\delta t}\left[2\sum_{\alpha=1}^{8}\boldsymbol{\tau}(\mathbf{x}-\mathbf{e}_\alpha\delta t,t)f_\alpha(\mathbf{x}-\mathbf{e}_\alpha\delta t,t)\right.\\
&\qquad -1.5\sum_{\alpha=1}^{8}\boldsymbol{\tau}(\mathbf{x},t)f_\alpha(\mathbf{x},t)\\
&\qquad \left.-\,0.5\sum_{\alpha=1}^{8}\boldsymbol{\tau}(\mathbf{x}-2\mathbf{e}_\alpha\delta t,t)f_\alpha(\mathbf{x}-2\mathbf{e}_\alpha\delta t,t)\right]\\
&\qquad + \Delta t\mathbf{A}_{\mathrm{rel-str}}(\boldsymbol{\tau},t).
\end{aligned} \tag{23}$$

C. The coupled LBGK model of extra force

The extra force must be treated appropriately to design the coupled LBM for the hydrodynamic of viscoelastic fluid. Here we apply the forced lattice Boltzmann BGK scheme [20] to treat the elastic force, as the same idea used in Ref. [21]. The effect of the elastic force is incorporated by adding the extra force $\mathbf{F} = \nabla\cdot\boldsymbol{\tau}$ into the momentum equation. The coupling way between the momentum equation and extra force is established by adding the following term F_α to the right-hand side of the evolution equation (5)

$$F_\alpha = \omega_\alpha\left[\frac{\mathbf{e}_\alpha\cdot\mathbf{M}}{c_s^2} + \frac{\mathbf{L}:\left(\mathbf{e}_\alpha\mathbf{e}_\alpha - c_s^2\mathbf{I}\right)}{2c_s^4}\right], \tag{24}$$

where

$$\mathbf{M} = \left(1-\frac{1}{2\lambda}\right)\mathbf{F}, \quad \mathbf{L} = \left(1-\frac{1}{2\lambda}\right)(\tilde{\mathbf{u}}\mathbf{F}+\mathbf{F}\tilde{\mathbf{u}}). \tag{25}$$

With this additional term, the incompressible LBGK Eq. (5) becomes

$$\begin{aligned}
&f_\alpha(\mathbf{x}+\mathbf{e}_\alpha\delta t,t+\delta t) - f_\alpha(\mathbf{x},t)\\
&\qquad = -\frac{1}{\lambda}\left[f_\alpha(\mathbf{x},t) - \tilde{f}_\alpha^{(\mathrm{eq})}\right] + \delta t F_\alpha,
\end{aligned} \tag{26}$$

where the equilibrium distribution $f_\alpha^{(\mathrm{eq})}$ is updated by

$$\tilde{f}_\alpha^{(\mathrm{eq})}(\mathbf{x},t) = E_\alpha(\tilde{\mathbf{u}}) = \begin{cases} \rho_0\left[1-(1-\omega_0)\frac{p}{\rho_0 c_s^2} + s_0(\tilde{\mathbf{u}})\right], & \alpha = 0,\\ \rho_0\left[\omega_\alpha\frac{p}{\rho_0 c_s^2} + s_\alpha(\tilde{\mathbf{u}})\right], & \alpha = 1,\ldots,8, \end{cases} \tag{27}$$

with

$$\tilde{\mathbf{u}}(\mathbf{r},t) = \sum_{\alpha=1}^{8}\mathbf{e}_\alpha f_\alpha(\mathbf{x}) + \frac{\delta t\mathbf{F}}{2\rho_0}. \tag{28}$$

Finally, the flow velocity is updated as an average value between the fore and after collision

$$\mathbf{u}(\mathbf{r},t) = \sum_{\alpha=1}^{8}\mathbf{e}_\alpha f_\alpha(\mathbf{x}) + \frac{\delta t\mathbf{F}}{2\rho_0}. \tag{29}$$

Finally, Eqs. (23) and (26) constitute a coupled system of the viscoelastic fluid described by the Oldroyd-B model.

D. The procedure and time marching of the coupled system

We will use the following procedure to simulate the velocity and viscoelastic stress fields. First, run Eq. (23) to solve the constitutive equation, and the results are used to determine the elastic force; next, the velocity fields are computed by using Eq. (26) and the results are used to compute the velocity gradient tensor. Sequentially, the viscoelastic stress and velocity fields are updated at each time step iteratively.

The lattice units are usually used in the traditional LBM. But one should note that the lattice units are not used in our method. We just intend to clarify the connections of two different scaling systems. At low Re number there is a large difference in the time scales between the momentum and stress tensor evolution to arrive at their steady states, which must be handled with care when modeling the real device.

We apply the asynchronously coupled method presented by E *et al.* [22] for the time marching of the coupled system. To distinguish the time scales and improve the computational stability, there are two time steps being used in the coupled LBM. The mesoscale model uses its own appropriate time step. The macro model runs at a slower pace than that required by the accuracy and stability consideration for the macroscale dynamic, in order for the mecro model to relax. The exchange of the data at every time step means that the mesoscale and macro models are asynchronously coupled. The computational savings come from the time scale separation. The mesoscale solver runs on a fictitious time scale, even though it has a small time step. The error introduced by the scale-separated condition is acceptable when the macro time step is chosen properly.

TABLE I. Comparison of memory requirements.

Method	Number of distribution functions to store			
	2DQ9 model		3DQ15 model	
	Distributions	Stress tensor	Distributions	Stress tensor
LBM with a single distribution	1×9	3	1×15	5
LBM with double distributions	$1 \times 9 + 3 \times 9$	3	$1 \times 15 + 5 \times 15$	5

The general algorithm for the single time step is presented as follows:

Require: $f_\alpha(\mathbf{x},t^n),\boldsymbol{\tau}(\mathbf{x},\tilde{t}^n),\delta t,\Delta t$

Do

$$f_\alpha(\mathbf{x},t^n+\delta t) \longrightarrow f_\alpha(\mathbf{x},t^n) - \frac{1}{\lambda}\left[f_\alpha(\mathbf{x},t^n) - \tilde{f}_\alpha^{(\mathrm{eq})}(\mathbf{x},t^n)\right] + \delta t F_\alpha;$$

$$F_\alpha = \psi(\boldsymbol{\tau}(\mathbf{x},\tilde{t}^n));$$

$$f_\alpha(\mathbf{x},t^{n+1}) \longrightarrow f_\alpha(\mathbf{x},t^n+\delta t);$$

$$\boldsymbol{\tau}(\mathbf{x},\tilde{t}^n+\Delta t) \longrightarrow \boldsymbol{\tau}(\mathbf{x},\tilde{t}^n) + \Delta t L(\boldsymbol{\tau}(\mathbf{x},\tilde{t}^n), f_\alpha(\mathbf{x},t^n+\delta t));$$

$$\boldsymbol{\tau}(\mathbf{x},\tilde{t}^{n+1}) \longrightarrow \boldsymbol{\tau}(\mathbf{x},\tilde{t}^n+\Delta t);$$

$$n \longrightarrow n+1;$$

While $n = T_n$.

E. Boundary conditions for the set of equations

Boundary conditions play an important role in LBM. For the wall or fully developed entry, we use the nonequilibrium extrapolation scheme proposed by Guo *et al.* [23] to treat the velocity boundary condition, which has the better numerical stability.

There is no boundary condition for the viscoelastic stress tensor to impose on the walls because of the domain as justified by the strong hyperbolic character of the constitutive equation, whereas the fully developed boundary condition is set for the entry. However, the performance of the scheme (23) is closely related to two points around them, so the issue of treatment near the boundary point is given as

$$\boldsymbol{\tau}(\tilde{\mathbf{x}},t+\Delta t) = \boldsymbol{\tau}(\tilde{\mathbf{x}},t) + \frac{\Delta t}{\delta t}\left[\sum_{\alpha=1}^{8}\boldsymbol{\tau}(\tilde{\mathbf{x}}-\mathbf{e}_\alpha\delta t,t) f_\alpha(\tilde{\mathbf{x}}-\mathbf{e}_\alpha\delta t,t) - \sum_{\alpha=1}^{8}\boldsymbol{\tau}(\tilde{\mathbf{x}},t) f_\alpha(\tilde{\mathbf{x}},t)\right] + \Delta t \mathbf{A}_{\mathrm{rel-str}}(\boldsymbol{\tau},t). \quad (30)$$

F. Remarks on the advantages of the present method

The primary advantage of the present method is that it involves smaller memory requirement compared with the LBM including two types of distribution functions [13,16]. Table I shows the comparison of memory requirements between the present method and LBM with two type distributions. From Table I we find that one has to store 6 sets of 15 distribution functions at each lattice point (for the 3DQ15 model), while the present approach just needs one set of distribution functions plus five independent components of the stress tensor. So the present method will allow us to simulate larger systems. Second, the particle distribution functions are directly used to treat the advection of the stress tensor, so it does not need to design special boundary conditions like Refs. [13] and [16]. Moreover, the new scheme of the constitutive equation presented in this paper can also improve the numerical accuracy. In addition, the time stepping for the coupled systems is more flexible, which could also keep some important advantages of LBM.

IV. NUMERICAL RESULTS AND DISCUSSIONS

We first validate the coupled LBM with the Oldroyd-B model by a planar channel flow, whose analytical solution can be easily obtained. Second, to test the capability of our numerical scheme for complex fluid, we consider the 4:1 contraction flow in Sec. IV B.

A. 2D channel flows

We consider a two-dimensional channel formed by two parallel plates at a distance h, and the length of the plate is $L = 10h$ (see Fig. 2). No-slip boundary conditions are assumed on the solid wall for the velocity. For the wall boundary conditions paralleling the x axis, the velocity conditions are as follows:

$$u_x = 0, \quad u_y = 0, \quad \frac{\partial u_y}{\partial x} = 0, \quad \frac{\partial u_y}{\partial y} = 0, \quad \frac{\partial u_x}{\partial x} = 0. \quad (31)$$

Then, the stress boundary conditions for the wall can be solved using those velocity equations of Eqs. (31). At the exit, the Neumann boundary conditions are imposed for the flow variables

$$\frac{\partial u_x}{\partial x} = 0, \quad \frac{\partial u_y}{\partial x} = 0, \quad \frac{\partial \tau_{xx}}{\partial x} = 0, \quad \frac{\partial \tau_{xy}}{\partial x} = 0, \quad \frac{\partial \tau_{yy}}{\partial x} = 0. \quad (32)$$

The fully developed conditions are used in the entry. Initially, the viscoelastic stress tensor is taken equal to zero

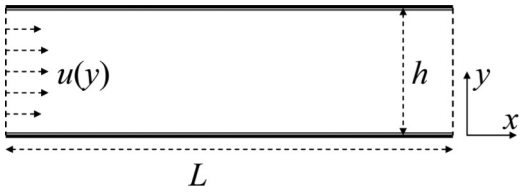

FIG. 2. Channel flow set up parameters.

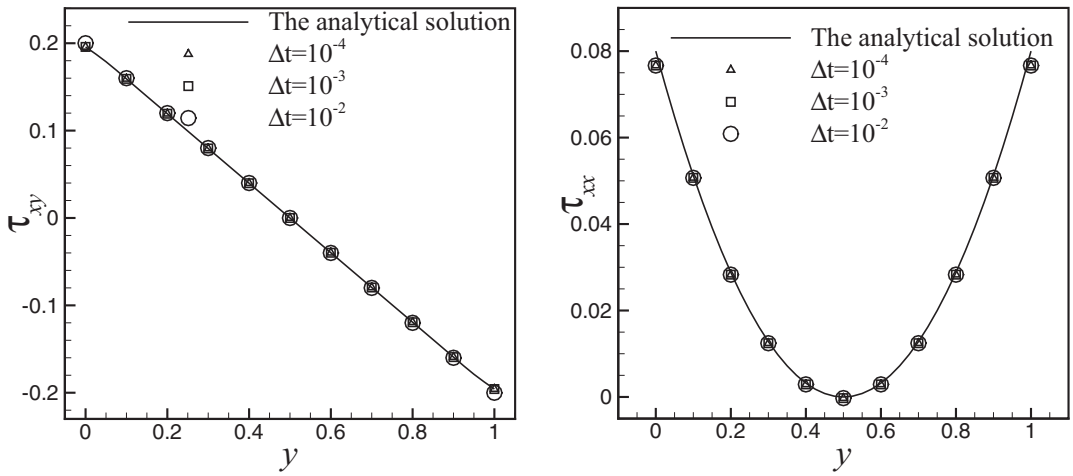

FIG. 3. The numerical solutions of the extra-stress component τ_{xy} (left) and normal-stress component τ_{xx} (right) at different time step: $\Delta t = 1.0 \times 10^{-4}$, 1.0×10^{-3}, 1.0×10^{-2} for $\mathrm{Wi} = 0.5$.

everywhere, and the velocity field is imposed by

$$u_x(0, y) = 0.4y(1 - y), \tag{33}$$

$$u_y = 0. \tag{34}$$

Under the steady state condition of the velocity field, there exist the analytical solutions for the Oldroyd-B constitutive equation which are given by

$$\tau_{xy} = (1 - \beta)\left(\frac{\partial u_x}{\partial y}\right), \tag{35}$$

$$\tau_{xx} - \tau_{yy} = 2\mathrm{Wi}(1 - \beta)\left(\frac{\partial u_x}{\partial y}\right)^2. \tag{36}$$

To validate the numerical scheme for the constitutive equation presented in this paper, we will compare our results with the analytical solutions. The analytical steady state solutions for the stress components have been given by Eqs. (35) and (36). As discussed in Sec. III D, the flow solver communicates with the stress solver at each time step. Namely, the constraint (i.e., the velocity gradient) on the constitutive equation changes at each step of stress solver while the instantaneous stress at each step is used to compute the flow field. To control the statistical error, we first discussed the choice of time step for the asynchronous coupling using a mesh of 300×30 with $\mathrm{Wi} = 0.5$. Our option is to run the stress solver with different macro time steps ($\Delta t = 1.0 \times 10^{-4}$, 1.0×10^{-3}, 1.0×10^{-2}) while keeping the time step δt fixed ($\delta t = 1.0 \times 10^{-5}$). Figure 3 shows the numerical results compared with the analytical solution. From Fig. 3 we see that the computational solution with $\Delta t = 1.0 \times 10^{-2}$ agrees very well with the analytical solution. We also see that the solution obtained using the smaller macro time steps ($\Delta t = 1.0 \times 10^{-4}$, 1.0×10^{-3}) has less affection, but this certainly increases the computational cost. Besides, if this diffusivity parameter is bigger than $\Delta t = 1.0 \times 10^{-2}$, the system has a very bad numerical accuracy. To find a compromise between computational cost and accuracy, we think that $\Delta t = 1.0 \times 10^{-2}$ is good enough for the simulation. In short, the coupled LBM with the asynchronous time marching could get a good result in our simulation when the

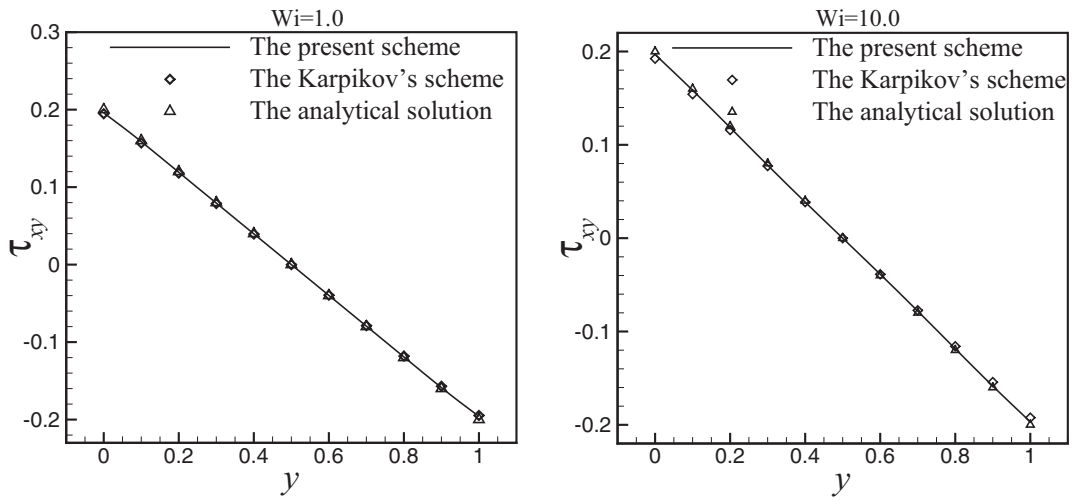

FIG. 4. Comparison of the presented scheme, Karpikov's scheme, and analytical solution of the profiles of the extra-stress component τ_{xy} with respect to the y at position $x = 5$ for $\mathrm{Wi} = 1.0$ (left), $\mathrm{Wi} = 10.0$ (right) with $\beta = 0.5$ and $\mathrm{Re} = 1.0$, respectively.

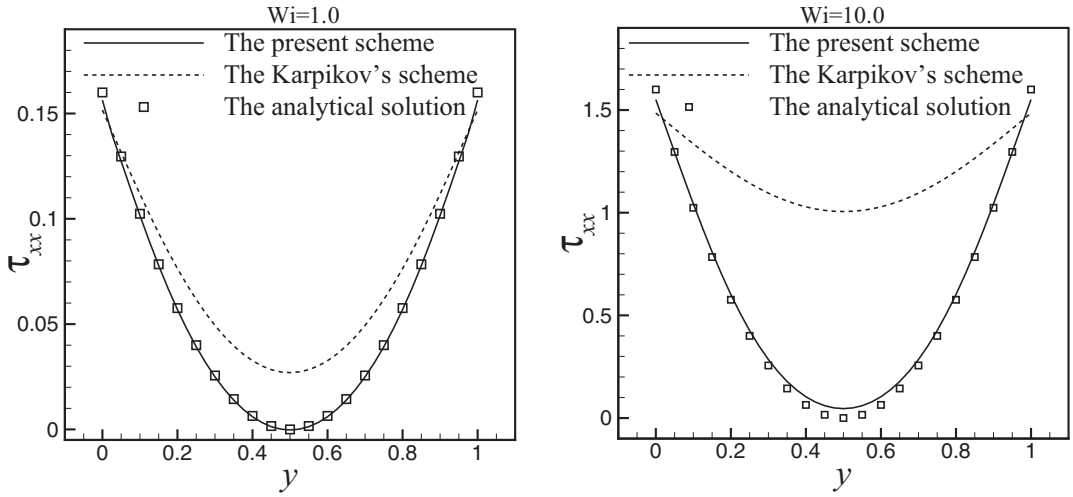

FIG. 5. Comparison of the presented scheme, Karpikov's scheme, and analytical solution of the profiles of the extra-stress component τ_{xx} with respect to the y at position $x = 5$ for Wi $= 1.0$ (left), Wi $= 10.0$ (right) with $\beta = 0.5$ and Re $= 1.0$, respectively.

macro time step is chosen properly. Second, we compare our results with those obtained by Karpikov's scheme to show the numerical accuracy of the presented method. As discussed above, we set $\delta t = 1.0 \times 10^{-5}$ and $\Delta t = 1.0 \times 10^{-2}$ for the following simulations using a mesh of 300×30. Figures 4 and 5 display the profiles of the extra-stress and normal-stress components with respect to the y axis at a position of $x = 5$ with $\beta = 0.5$, Re $= 1.0$, and Wi $= 1.0$, Wi $= 10.0$, respectively. As can be seen in Figs. 4 and 5, the numerical results of extra-stress and normal-stress components solved by the presented scheme agree well with the analytical solutions. But from Fig. 4 we find that the numerical results of the normal-stress component obtained by Karpikov's scheme deviate seriously from the analytical solution. In other words, there is considerable numerical dissipation for Karpikov's scheme when it is used to solve the normal-stress component.

For a further explanation of all the points made above, we then discuss the numerical accuracy of the stress tensor in the following. We define $E(\tau_{xy})$ and $E(\tau_{xx})$ as the relative L_2-norm errors for the numerical solutions of the stress components, which are calculated by using the following formulas:

$$E(\tau_{xy}) = \sqrt{\frac{\sum_{k=1}^{M}\left[\tau_{xy}^{\text{exact}}(\mathbf{x}_k) - \tau_{xy}^{\text{numerical}}(\mathbf{x}_k)\right]^2}{\sum_{k=1}^{M}\tau_{xy}^{\text{exact}}(\mathbf{x}_k)^2}}, \tag{37}$$

$$E(\tau_{xx}) = \sqrt{\frac{\sum_{k=1}^{M}\left[\tau_{xx}^{\text{exact}}(\mathbf{x}_k) - \tau_{xx}^{\text{numerical}}(\mathbf{x}_k)\right]^2}{\sum_{k=1}^{M}\tau_{xx}^{\text{exact}}(\mathbf{x}_k)^2}}, \tag{38}$$

where M is the total number of lattice cells; $\tau_{xy}^{\text{numerical}}$ and $\tau_{xx}^{\text{numerical}}$ are the numerical solutions that have converged to the steady state; and τ_{xy}^{exact} and τ_{xx}^{exact} are the exact steady state solutions. Figures 6 and 7 show the relative L_2-norm

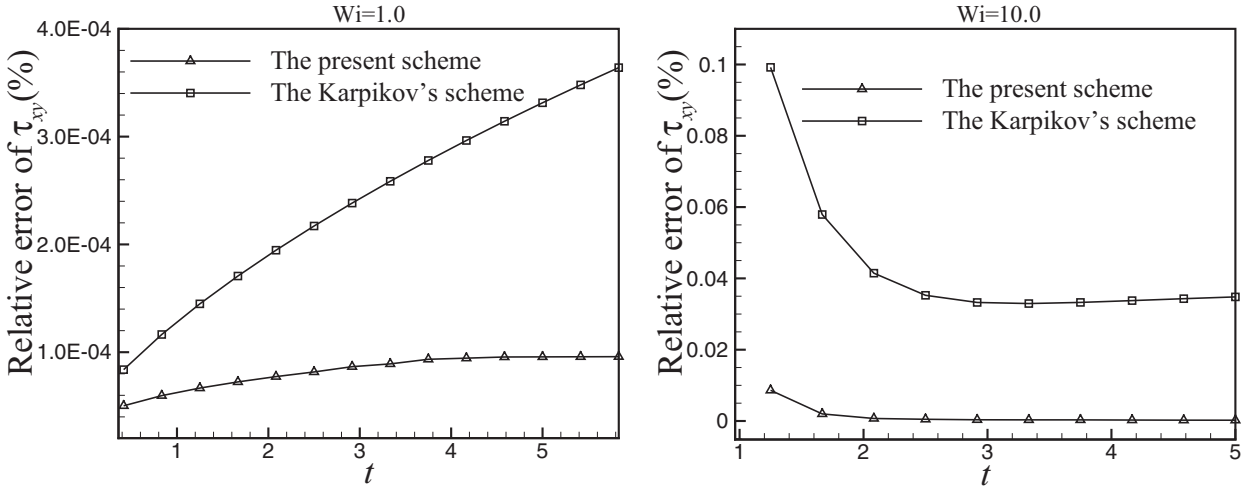

FIG. 6. Comparison of the relative L_2 error of the extra-stress component τ_{xy} between the presented scheme and Karpikov's scheme with respect to the time t for Wi $= 1.0$ (left), Wi $= 10.0$ (right) with $\beta = 0.5$ and Re $= 1.0$, respectively.

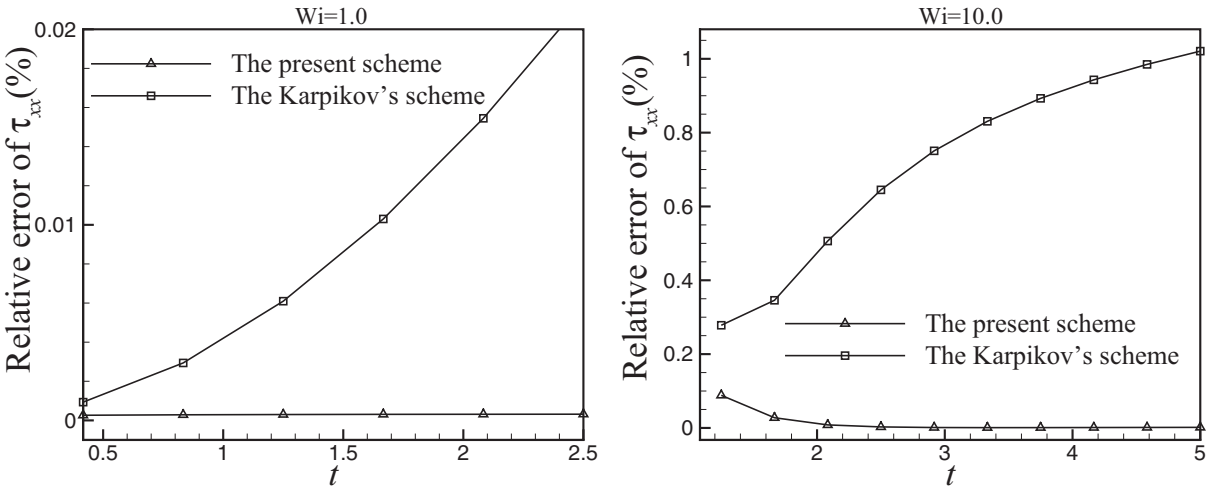

FIG. 7. Comparison of the relative L_2 error of the extra-stress component τ_{xx} between the presented scheme and Karpikov's scheme with respect to the time t for Wi = 1.0 (left), Wi = 10.0 (right) with $\beta = 0.5$ and Re = 1.0, respectively.

errors of the extra-stress component τ_{xy} and the normal-stress component τ_{xx} with respect to time t with $\beta = 0.5$ and Re = 1.0 for Wi = 1.0, Wi = 10.0, respectively. From Fig. 6 we can see that the relative L_2-norm error of τ_{xy} is extremely small for both Karpikov's scheme and the present scheme for Wi = 1.0. Figure 7 shows that the relative L_2-norm error of τ_{xx} is less than 0.1% at $t = 2.5$ for our present scheme for Wi = 1.0, whereas the relative L_2-norm error of Karpikov's scheme is more than 2.0%. Particularly, as the Wi number increased from 1.0 to 10.0, the relative L_2-norm error obtained by Karpikov's scheme is clearly to exceed more than 100.0%. Overall, through the analysis of the relative L_2-norm error mentioned above, we find that the present scheme for the constitutive equation has a low numerical dissipation. So there is a significant improvement of the numerical accuracy of the normal-stress component, in particular at high Wi.

Figure 8 plots the numerical results of the evolution for u_x at the central point (5, 0.5) with respect to time t at $\beta = 0.5$ and Re = 1.0 for Wi = 1.0 and 10.0, respectively. From Fig. 8 it is of interest to note that with increasing time u_x overshoot the terminal velocity before eventually tending to the end state, because of the effect on the flow through a channel including the elasticity. More importantly, at a higher Wi = 10.0, the numerical results solved by our proposed scheme show the velocity overshoot before tending to that terminal velocity for a sufficiently long time. However, we also find that the effect on the velocity including the elasticity obtained by Karpikov's scheme is much weaker than that of the scheme presented in this paper, perhaps this is due to its numerical dissipation. The overshoot behavior of viscoelastic liquid in the unsteady flow has been noted before, theoretically by Fielder and Thomas [24], Hermes and Fredrickson [25], and Water and King [26]. The numerical results obtained by our new scheme are found to be in good agreement with those previous studies. As expected, the viscoelastic fluid exhibits the more complex rheology behavior, which is different from that of the Newtonian fluid.

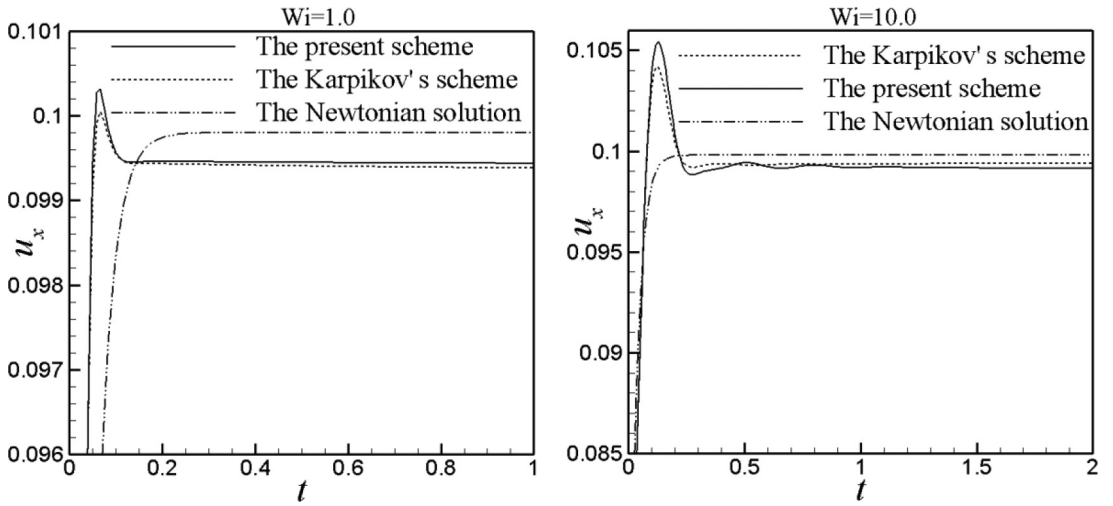

FIG. 8. The evolution of the velocity component u_x at a central point (5, 0.5) with respect to the time t for Wi = 1.0 (left), Wi = 10.0 (right) with $\beta = 0.5$ and Re = 1.0, respectively.

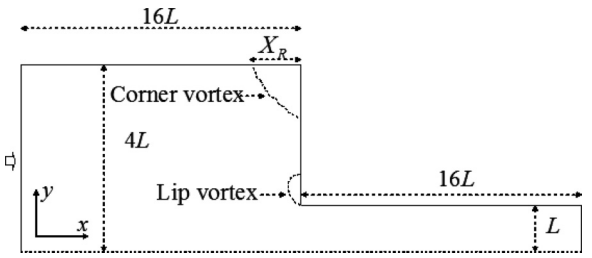

FIG. 9. Schematic of half the planar 4:1 contraction flow.

B. Flow through the 4:1 planar contraction

The flow through the contraction geometry has some key complex features, which is involved in the polymer processing such as the combination of the shear and extensional deformations. Therefore, it is recognized as an ideal benchmark problem for both the experimental and numerical studies of complex viscoelastic fluid. In this section we try to simulate the Oldroyd-B fluid in contraction geometry using the method presented in this paper. The flow domain is shown in Fig. 9. The line $y = 0$ is a mirror plane in the system so we only model the top half. The ratio of the half height of downstream and upstream channel is set to 4, which generates the complex flow exhibiting strong shearing near the walls and planar extension along the centerline. We choose the dimensionless units $U = 1$ and $L = 1$, then $\mathrm{Wi} = \lambda_p$.At inflow, a fully developed parabolic Poiseuille flow is imposed by

$$u_x = \frac{3}{128}(16 - y^2), \quad u_y = 0, \tag{39}$$

while the Neumann boundary conditions are given at the outlet under the assumption of the fully developed conditions. No-slip boundary conditions are imposed along the stationary walls. Symmetry boundary conditions are imposed along the centerline. We take the dimensionless parameter β as $1/9$, and Re number as 1.0. To compare the results with the reference data published in the literature, we define the distance between the points, where the separation line meets the bottom of the channel and the salient corner, as salient vortex length X_R. As discussed in the channel flow, we also need to be cautious with the choice of time step for the asynchronous coupling. We note that the solution obtained by using small macro time step ($\Delta t < 5.0 \times 10^{-4}$) has less affection for $\mathrm{Wi} < 2.5$ in the simulation. For the compromise between the computational cost and accuracy, we set $\delta t = 1.0 \times 10^{-5}$ for $\mathrm{Re} = 1.0$, and $\Delta t = 5.0 \times 10^{-4}$ in this section.

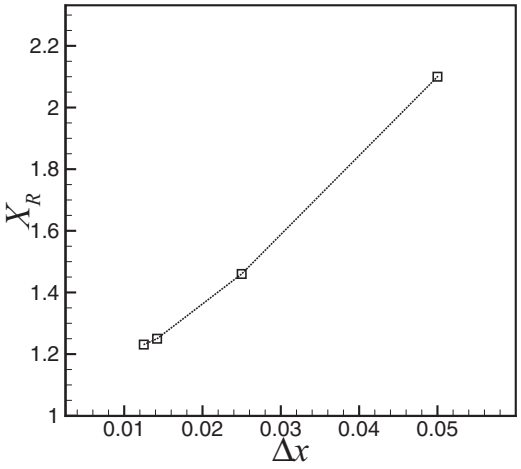

FIG. 11. Convergence of predicted X_R with mesh refinement at $\mathrm{Wi} = 0.5$.

We perform the numerical calculations on a series of meshes to ensure that the simulated solutions are independent of mesh. The characteristics of the four meshes are shown in Table II. Figure 10 shows the effect of the mesh refinement on the streamline patterns at $\mathrm{Wi} = 0.5$. The strength of the lip vortex decreases as the mesh is refined, which suggests that the lip vortex is sensitive to the mesh refinement. The result of Matallah *et al.* [27] also suggested that the lip vortex was sensitive to mesh size. Figure 11 demonstrates the convergence of X_R with mesh refinement at $\mathrm{Wi} = 0.5$. It could be observed that the range of variation for X_R is to be minimal with the mesh M4. So, we use the mesh M4 in the following calculations to find a compromise between the computational cost and accuracy.

Figure 12 displays the streamline patterns with four different Wi numbers. It is noted that the lip vortex emerges and grows up as Wi is increased; the lip vortex first appears about at $\mathrm{Wi} = 1.0$, but cannot be clearly observed without zooming until $\mathrm{Wi} \geqslant 2.0$. In the result of [27], a weak lip vortex was also detected for $\mathrm{Wi} \geqslant 2.0$. In the experimental works, the lip vortex enhancement was observed for shear-thinning fluid in planar 4:1 contraction flow [28]. Though Nigen and

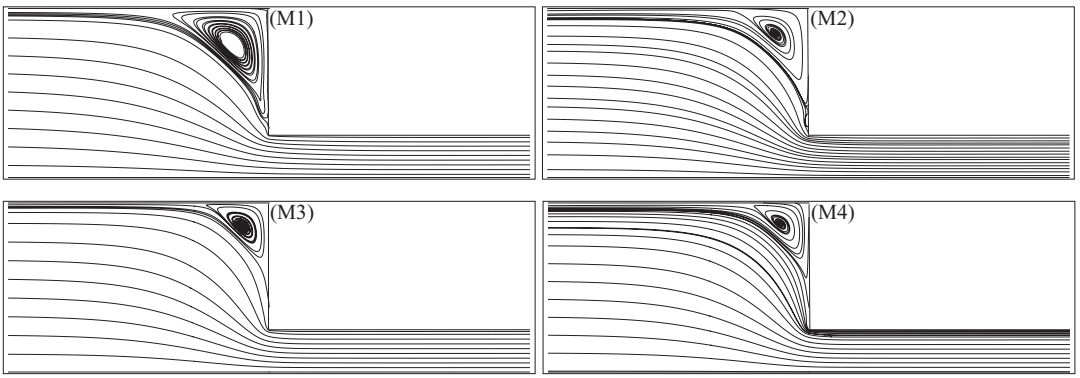

FIG. 10. Mesh dependence of streamlines at $\mathrm{Wi} = 0.5$ using a mesh of M1, M2, M3, and M4.

TABLE II. Mesh characteristics used in this study.

Mesh	Total cell	Δx
M1	120 000	0.05
M2	128 000	0.025
M3	392 000	0.0142
M4	512 000	0.0125

Walters [29] did not observe the steady lip vortex, they reported the temporal existence of the lip vortex just before the flow instability occurred.

Figure 13 displays the value of the salient vortex length with different Wi numbers using the finer mesh M4, compared with those data in the literature [27,30]. It appears that the salient vortex length predicted by the present method decreases as Wi increases for Wi $\leqslant$ 2.0. As can be seen from Fig. 13, the salient vortex length given by the present coupled method agrees well with the reference solutions reported by Matallah *et al*. [27] using the finite element method. On the other hand, although the present results are slightly higher than those using a semi-Lagrangian finite volume scheme [30], they show the same decreased trend of vortex size as Wi increased. Again, the values of the salient vortex length exhibit the similar behaviors to those obtained for Re = 0.0 in Ref. [31]. However, we notice that the value of X_R obtained by Karpikov's scheme is significantly different from the other results, perhaps because of its numerical dissipation.

Figure 14 depicts the three components of the stress tensor at the steady state for Wi = 1.0. The results calculated by the present coupled LBM show that there is a buildup of stress boundary layers near downstream of the re-entrant corner, while the contours are smooth around the corner singularity. Moreover, a region of high stress concentration is observed beyond the re-entrant corner on the downstream channel wall for both τ_{xy} and τ_{xx}. These structural features of the stress tensor are qualitatively similar to those of Aboubacar *et al*. in [32]. Finally, Fig. 15 shows the numerical solutions of the velocity component through the horizontal centerline of the planar contraction for Wi = 0.0, 2.0, respectively. It can be seen clearly that the velocity overshoot is so apparent with increasing elasticity (Wi = 2.0). Since the elongational flow is dominant along the centerline, the accelerating velocity can be attributed to the sharp gradient of the longitudinal normal

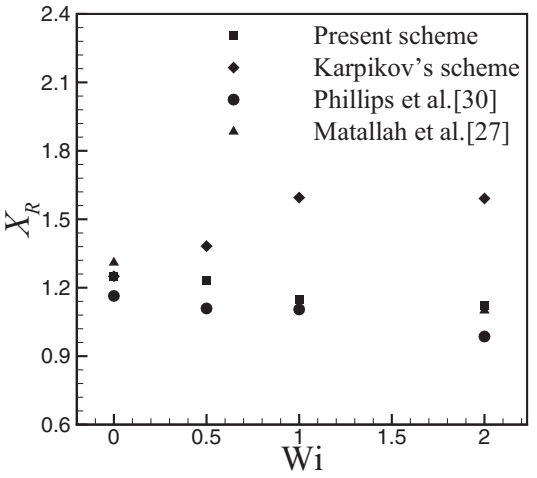

FIG. 13. The values of the salient vortex lengths with different Wi numbers comparing with those data taken from the literature.

stress. This feature agrees qualitatively with that of [33], which observed the similar behavior of the creeping flow at Wi = 2.5.

V. CONCLUSIONS

In summary, we have developed a lattice Boltzmann method coupled with the Oldroyd-B constitutive equation to simulate the viscoelastic fluid in the context of a single distribution function. In our method, the flow field of the solvent is solved by using a 2D incompressible lattice Boltzmann BGK model, whereas the advection operator of the polymer stress tensor is directly calculated with the help of the particle distribution functions. Specifically, to improve the numerical accuracy of the simulation, we presented a numerical scheme for the advection of stress tensor through the truncation of second-order Taylor expansion. We have found that our method could greatly ease the numerical dissipation of the simulation for the stress tensor. The numerical results of 2D channel flow agree well with the analytical and some experiment results reported in the previous studies. Furthermore, we have also shown that our method could capture some complex rheological behaviors of the 4:1 contraction flow.

Unlike the LBM including two types of distribution functions, the coupled LBM presented in this paper has the advantage of smaller memory requirements. So the new

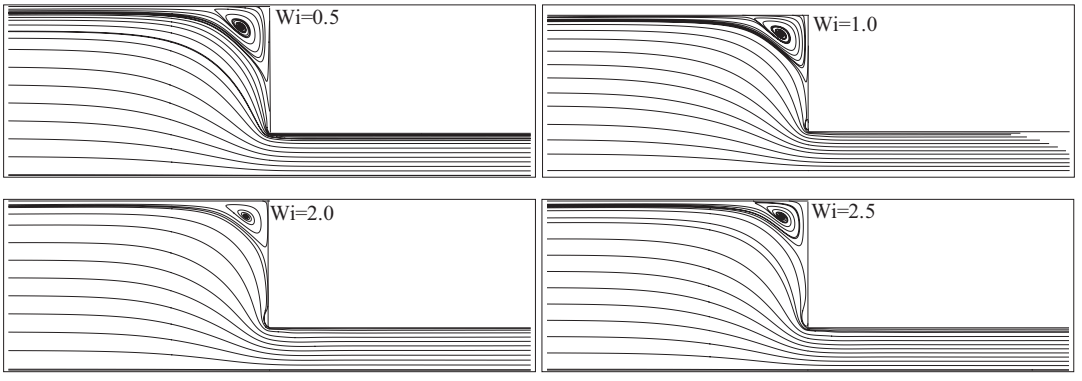

FIG. 12. The streamlines for different Wi numbers: Wi = 0.5, 1.0, 2.0, and 2.5.

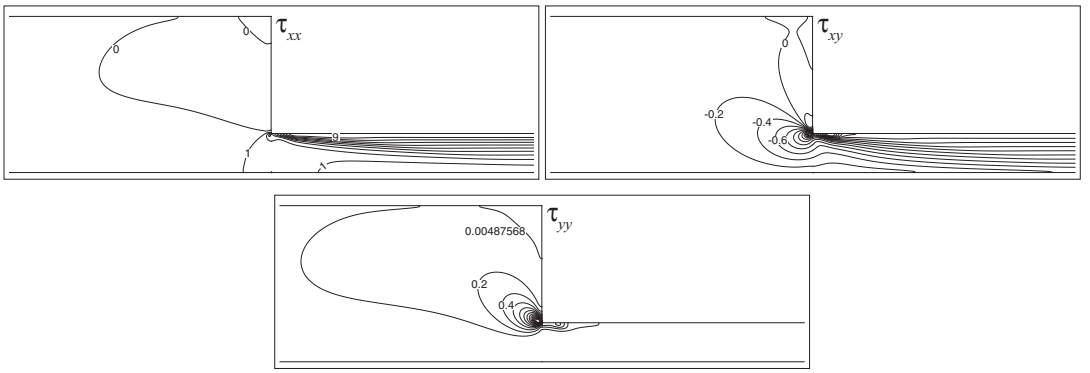

FIG. 14. The stress contours of τ_{xx}, τ_{xy}, and τ_{yy} for Wi = 1.0.

method may allow us to simulate large systems. Moreover, our algorithm automatically maintains the traditional advantages of LBM without extra enforcement, and could also be easily implemented. Nevertheless, some important issues, such as the investigations of other more sophisticated constitutive equations and elastic instability behaviors, are needed to study further, which would contain the more physical ingredients.

ACKNOWLEDGMENTS

We thankfully acknowledge the support of the National Basic Research Program of China (Grant No. 2012CB025903), the Northwestern Polytechnical University Foundation for Fundamental Research (JCY20130141) and the Natural Science Foundation of Shanxi Province (Grant No. 2012011019-2). Many thanks go to Lin Zhang (Institute of Process Engineering, Chinese Academy of Sciences) for polishing the article.

APPENDIX: THE DERIVATION OF THE NUMERICAL SCHEME FOR ADVECTION OPERATOR

In this Appendix we show the derivation of the new scheme for the advection operator of a polymer stress tensor. The idea is to calculate the advection operator appropriately by truncating the Taylor series expansion. We will derive that

$$\begin{aligned}\delta t\mathbf{A}_{\rm adv}(\boldsymbol{\tau},t) \approx\ & 2\sum_{\alpha=1}^{m}\boldsymbol{\tau}(\mathbf{x}-\mathbf{e}_\alpha\delta t,t)f_\alpha(\mathbf{x}-\mathbf{e}_\alpha\delta t,t)\\ & -1.5\sum_{\alpha=1}^{m}\boldsymbol{\tau}(\mathbf{x},t)f_\alpha(\mathbf{x},t)\\ & -0.5\sum_{\alpha=1}^{m}\boldsymbol{\tau}(\mathbf{x}-2\mathbf{e}_\alpha\delta t,t)f_\alpha(\mathbf{x}-2\mathbf{e}_\alpha\delta t,t),\end{aligned} \tag{A1}$$

where $\mathbf{A}_{\rm adv}(\boldsymbol{\tau},t)=(\mathbf{u}\cdot\nabla)\boldsymbol{\tau}$ is the advection operator applied to polymer stress tensor $\boldsymbol{\tau}$; and $f_\alpha(\mathbf{x},t)$ is the distribution function at node $\mathbf{x}$ at a time t.

According to the two-dimensional nine velocity (D2Q9) model, the macroscopic flow velocity is computed from the distribution functions as follows:

$$u_i(\mathbf{x},t)=\sum_{\alpha=1}^{8}(\mathbf{e}_\alpha)_i f_\alpha(\mathbf{x}), \tag{A2}$$

$$\delta t\mathbf{A}_{\rm adv}(\boldsymbol{\tau},t)=\delta t\frac{\partial}{\partial x_i}\left[\boldsymbol{\tau}(\mathbf{x},t)u_i(\mathbf{x},t)\right]. \tag{A3}$$

Substituting Eq. (A2) into Eq. (A3) we get

$$\begin{aligned}\delta t\mathbf{A}_{\rm adv}(\boldsymbol{\tau},t) &= \delta t\frac{\partial}{\partial x_i}\left[\boldsymbol{\tau}(\mathbf{x},t)u_i(\mathbf{x},t)\right]\\ &= \delta t\frac{\partial}{\partial x_i}\boldsymbol{\tau}(\mathbf{x},t)\sum_{\alpha=1}^{8}f_\alpha(\mathbf{x},t)(\mathbf{e}_\alpha)_i\\ &= \frac{\partial}{\partial x_i}\sum_{\alpha=1}^{8}\boldsymbol{\tau}(\mathbf{x},t)f_\alpha(\mathbf{x},t)(\mathbf{e}_\alpha)_i\delta t.\end{aligned} \tag{A4}$$

Now, the Taylor expansion of the function $\sum_{\alpha=1}^{m}\boldsymbol{\tau}(\mathbf{x}-\mathbf{e}_\alpha\delta t,t)f_\alpha(\mathbf{x}-\mathbf{e}_\alpha\delta t,t)$, about $\mathbf{x}$, may be approximated,

$$\begin{aligned}&\sum_{\alpha=1}^{m}\boldsymbol{\tau}(\mathbf{x}-\mathbf{e}_\alpha\delta t,t)f_\alpha(\mathbf{x}-\mathbf{e}_\alpha\delta t,t)\\ &=\sum_{\alpha=1}^{m}\boldsymbol{\tau}(\mathbf{x},t)f_\alpha(\mathbf{x},t)-\frac{\partial}{\partial x_i}\sum_{\alpha=1}^{m}\boldsymbol{\tau}(\mathbf{x},t)f_\alpha(\mathbf{x},t)(\mathbf{e}_\alpha)_i\delta t\\ &\quad+0.5\frac{\partial^2}{\partial x_i\partial x_j}\sum_{\alpha=1}^{m}\boldsymbol{\tau}(\mathbf{x},t)f_\alpha(\mathbf{x},t)(\mathbf{e}_\alpha)_i(\mathbf{e}_\alpha)_j(\delta t)^2+o(\delta t)^2.\end{aligned} \tag{A5}$$

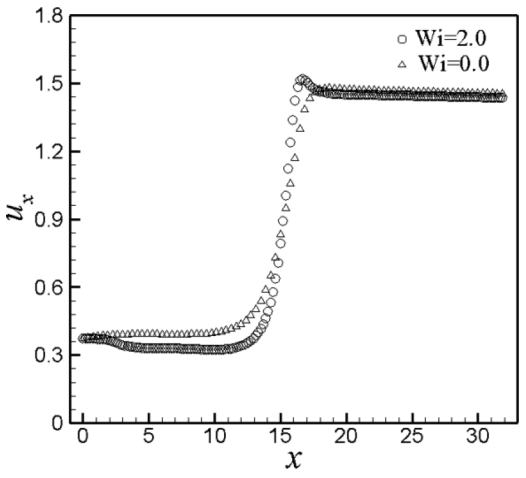

FIG. 15. Velocity overshoots along symmetric line.

Then, the Taylor expansion of the function $\sum_{\alpha=1}^{m}\boldsymbol{\tau}(\mathbf{x}-2\mathbf{e}_\alpha\delta t,t)f_\alpha(\mathbf{x}-2\mathbf{e}_\alpha\delta t,t)$, about $\mathbf{x}$, may be also approximated,

$$\begin{aligned}&\sum_{\alpha=1}^{m}\boldsymbol{\tau}(\mathbf{x}-2\mathbf{e}_\alpha\delta t,t)f_\alpha(\mathbf{x}-2\mathbf{e}_\alpha\delta t,t)\\&=\sum_{\alpha=1}^{m}\boldsymbol{\tau}(\mathbf{x},t)f_\alpha(\mathbf{r},t)-\frac{\partial}{\partial x_i}\sum_{\alpha=1}^{m}\boldsymbol{\tau}(\mathbf{x},t)f_\alpha(\mathbf{x},t)(\mathbf{e}_\alpha)_i(2\delta t)\\&\quad+0.5\frac{\partial^2}{\partial x_i\partial x_j}\sum_{\alpha=1}^{m}\boldsymbol{\tau}(\mathbf{x},t)f_\alpha(\mathbf{x},t)(\mathbf{e}_\alpha)_i(\mathbf{e}_\alpha)_j(2\delta t)^2+o(\delta t)^2.\end{aligned}\tag{A6}$$

Equation (A5) is multiplied by factor 2, and then substitutes Eq. (A5) $\times$ 2 into Eq. (A6), we can rewrite Eq. (A6) as

$$\begin{aligned}&0.5\frac{\partial^2}{\partial x_i\partial x_j}\sum_{\alpha=1}^{m}\boldsymbol{\tau}(\mathbf{x},t)f_\alpha(\mathbf{x},t)(\mathbf{e}_\alpha)_i(\mathbf{e}_\alpha)_j(\delta t)^2\\&=\sum_{\alpha=1}^{m}\boldsymbol{\tau}(\mathbf{x}-\mathbf{e}_\alpha\delta t,t)f_\alpha(\mathbf{x}-\mathbf{e}_\alpha\delta t,t)-0.5\sum_{\alpha=1}^{m}\boldsymbol{\tau}(\mathbf{x},t)f_\alpha(\mathbf{x},t)\\&\quad-0.5\sum_{\alpha=1}^{m}\boldsymbol{\tau}(\mathbf{x}-2\mathbf{e}_\alpha\delta t,t)f_\alpha(\mathbf{x}-2\mathbf{e}_\alpha\delta t,t)+o(\delta t)^2.\end{aligned}\tag{A7}$$

Using (A3)–(A7) we have

$$\begin{aligned}&-\delta t\frac{\partial}{\partial x_i}\left[\boldsymbol{\tau}(\mathbf{x},t)u_i(\mathbf{x},t)\right]\\&=\sum_{\alpha=1}^{m}\boldsymbol{\tau}(\mathbf{x}-\mathbf{e}_\alpha\delta t,t)f_\alpha(\mathbf{x}-\mathbf{e}_\alpha\delta t,t)-\sum_{\alpha=1}^{m}\boldsymbol{\tau}(\mathbf{x},t)f_\alpha(\mathbf{x},t)\\&\quad-0.5\frac{\partial^2}{\partial x_i\partial x_j}\sum_{\alpha=1}^{m}\boldsymbol{\tau}(\mathbf{x},t)f_\alpha(\mathbf{x},t)(\mathbf{e}_\alpha)_i(\mathbf{e}_\alpha)_j(\delta t)^2+o(\delta t)^2\\&=\sum_{\alpha=1}^{m}\boldsymbol{\tau}(\mathbf{x}-\mathbf{e}_\alpha\delta t,t)f_\alpha(\mathbf{x}-\mathbf{e}_\alpha\delta t,t)-\sum_{\alpha=1}^{m}\boldsymbol{\tau}(\mathbf{x},t)f_\alpha(\mathbf{x},t)\\&\quad+\sum_{\alpha=1}^{m}\boldsymbol{\tau}(\mathbf{x}-\mathbf{e}_\alpha\delta t,t)f_\alpha(\mathbf{x}-\mathbf{e}_\alpha\delta t,t)\\&\quad-0.5\sum_{\alpha=1}^{m}\boldsymbol{\tau}(\mathbf{x},t)f_\alpha(\mathbf{x},t)\\&\quad-0.5\sum_{\alpha=1}^{m}\boldsymbol{\tau}(\mathbf{x}-2\mathbf{e}_\alpha\delta t,t)f_\alpha(\mathbf{x}-2\mathbf{e}_\alpha\delta t,t)+o(\delta t)^2.\end{aligned}\tag{A8}$$

Using the continuity equation and incompressibility of the fluid

$$\frac{\partial}{\partial x_i}u_i(\mathbf{x},t)=0.\tag{A9}$$

We get

$$\begin{aligned}\frac{\partial}{\partial x_i}\left[\boldsymbol{\tau}(\mathbf{x},t)u_i(\mathbf{x},t)\right]&=u_i(\mathbf{x},t)\frac{\partial}{\partial x_i}\boldsymbol{\tau}(\mathbf{x},t)+\boldsymbol{\tau}(\mathbf{x},t)\frac{\partial}{\partial x_i}u_i(\mathbf{x},t)\\&=u_i(\mathbf{x},t)\frac{\partial}{\partial x_i}\boldsymbol{\tau}(\mathbf{x},t).\end{aligned}\tag{A10}$$

Combining Eqs. (A8) and (A10) and casting out the term of truncation error $o(\delta t)^2$, we get

$$\begin{aligned}\delta t\mathbf{A}_{\mathrm{adv}}(\boldsymbol{\tau},t)&=\delta t\frac{\partial}{\partial x_i}\left[\boldsymbol{\tau}(\mathbf{x},t)u_i(\mathbf{x},t)\right]\\&\approx 2\sum_{\alpha=1}^{m}\boldsymbol{\tau}(\mathbf{x}-\mathbf{e}_\alpha\delta t,t)f_\alpha(\mathbf{x}-\mathbf{e}_\alpha\delta t,t)\\&\quad-1.5\sum_{\alpha=1}^{m}\boldsymbol{\tau}(\mathbf{x},t)f_\alpha(\mathbf{x},t)\\&\quad-0.5\sum_{\alpha=1}^{m}\boldsymbol{\tau}(\mathbf{x}-2\mathbf{e}_\alpha\delta t,t)f_\alpha(\mathbf{x}-2\mathbf{e}_\alpha\delta t,t).\end{aligned}\tag{A11}$$

[1] S. Succi, *The Lattice Boltzmann Equation for Fluid Dynamics and Beyond* (Oxford University Press, Oxford, 2001).
[2] Y. H. Qian, D. d'Humières, and P. Lallemand, Europhys. Lett. **17**, 479 (1992).
[3] S. Chen and G. D. Doolen, Annu. Rev. Fluid Mech. **30**, 329 (1998).
[4] Y. H. Qian and Y. F. Deng, Phys. Rev. Lett. **79**, 2742 (1997).
[5] L. Giraud, D. d'Humières, and P. Lallemand, Int. J. Mod. Phys. C **8**, 805 (1997).
[6] L. Giraud, D. d'Humières, and P. Lallemand, Europhys. Lett. **42**, 625 (1998).
[7] P. Lallemand, D. d'Humières, L. S. Luo, and R. Rubinstein, Phys. Rev. E **67**, 021203 (2003).
[8] A. J. Wagner, L. Giraud, and C. E. Scott, Comput. Phys. Commun. **129**, 227 (2000).
[9] I. Ispolatov and M. Grant, Phys. Rev. E **65**, 056704 (2002).
[10] J. Onishi, Y. Chen, and H. Ohashi, Phys. A **362**, 84 (2006).
[11] A. Ammar, J. Non-Newtonian Fluid Mech. **165**, 1082 (2010).
[12] T. N. Phillips and G. W. Roberts, IMA J. Appl. Math. **76**, 790 (2011).
[13] O. Malaspinasa, N. Fiétier, and M. Devillea, J. Non-Newtonian Fluid Mech. **165**, 1637 (2010).
[14] C. Denniston, E. Orlandini, and J. M. Yeomans, Phys. Rev. E **63**, 056702 (2001).
[15] T. J. Spencer and C. M. Care, Phys. Rev. E **74**, 061708 (2006).
[16] J. Su, J. Ouyang, X. Wang, B. Yang, and W. Zhou, J. Non-Newtonian Fluid Mech. **194**, 42 (2013).
[17] A. Karpikov, Ph.D. thesis, Yale University, 2005.
[18] R. Bird, C. Curtiss, R. Armstrong, and O. Hassager, *Dynamics of Polymeric Liquids*, Vols. 1 and 2 (Wiley, New York, 1987).
[19] Z. L. Guo, B. C. Shi, and N. C. Wang, J. Comput. Phys. **165**, 288 (2000).
[20] Z. L. Guo, C. G. Zheng, and B. C. Shi, Phys. Rev. E **65**, 046308 (2002).
[21] B. C. Shi, Z. L. Guo, and C. G. Zheng, Int. J. Numer. Meth. Fluids **39**, 325 (2002).

[22] W. E, W. Q. Ren, and E. Vanden-Eijnden, J. Comput. Phys. **228**, 5437 (2009).
[23] Z. L. Guo, C. G. Zheng, and B. C. Shi, Chin. Phys. **11**, 366 (2002).
[24] R. Fielder and R. H. Thomas, Rheol. Acta **6**, 306 (1967).
[25] R. A. Hermes and A. G. Fredriekson, AIChE J. **13**, 253 (1967).
[26] N. D. Waters and M. J. King, Rheol. Acta **9**, 345 (1970).
[27] H. Matallah, P. Townsend, and M. F. Webster, J. Non-Newtonian Fluid Mech. **75**, 139 (1998).
[28] R. E. Evans and K. Walters, J. Non-Newtonian Fluid Mech. **32**, 95 (1989).
[29] S. Nigen and K. Walters, J. Non-Newtonian Fluid Mech. **102**, 343 (2002).
[30] T. N. Phillips and A. J. Williams, J. Non-Newtonian Fluid Mech. **87**, 215 (1999).
[31] M. A. Alves, P. J. Oliveira, and F. T. Pinho, J. Non-Newtonian Fluid Mech. **110**, 45 (2003).
[32] M. Aboubacar, H. Matallah, and M. F. Webster, J. Non-Newtonian Fluid Mech. **103**, 65 (2002).
[33] J. M. Kimb, C. Kimb, J. H. Kimc, C. Chunga, K. H. Ahna, and S. J. Lee, J. Non-Newtonian Fluid Mech. **129**, 23 (2005).